Structure of the Baroclinic Tide Generated at Kaena Ridge, Hawaii

JONATHAN D. NASH

College of Oceanic and Atmospheric Sciences, Oregon State University, Corvallis, Oregon

ERIC KUNZE

School of Earth and Ocean Sciences, University of Victoria, Victoria, British Columbia, Canada

CRAIG M. LEE AND THOMAS B. SANFORD

Applied Physics Laboratory and School of Oceanography, University of Washington, Seattle, Washington

(Manuscript received 2 April 2004, in final form 5 October 2005)

ABSTRACT

Repeat transects of full-depth density and velocity are used to quantify generation and radiation of the semidiurnal internal tide from Kaena Ridge, Hawaii. A 20-km-long transect was sampled every 3 h using expendable current profilers and the absolute velocity profiler. Phase and amplitude of the baroclinic velocity, pressure, and vertical displacement were computed, as was the energy flux. Large barotropically induced isopycnal heaving and strong baroclinic energy-flux divergence are observed on the steep flanks of the ridge where upward and downward beams radiate off ridge. Directly above Kaena Ridge, strong kinetic energy density and weak net energy flux are argued to be a horizontally standing wave. The phasing of velocity and vertical displacements is consistent with this interpretation. Results compare favorably with the Merrifield and Holloway model.

1. Introduction

Interest in internal tides has been revived by recognition that up to one-third of the surface tide dissipation occurs in the deep ocean (Egbert and Ray 2001; Kantha and Tierney 1997) and that this tidal energy could contribute significantly to the roughly 2 TW of abyssal mixing thought to be needed to close the upwelling branch of the meridional thermohaline circulation (Munk and Wunsch 1998); the remainder presumably comes from wind forcing into near-inertial motions (e.g., Alford 2003) and into the mean flow (Wunsch 1998). Assimilating satellite altimetry data into a barotropic tide model, Egbert and Ray (2001) found that 0.8 TW of the surface tide was lost at ridges, trenches, and island chains in the deep ocean. Two-layer numerical simulations (Simmons et al. 2004) show that 75% of the deep-ocean surface tide loss enters the low-mode wave field through just 12 regions of abrupt topography. Satellite altimetry also reveals low-mode internal tides radiating from these same topographic features (Ray and Mitchum 1997). While most tide–topography interaction theory is posed in the weak-amplitude limit with subcritical slopes and small heights (Bell 1975; St. Laurent and Garrett 2002; Llewellyn Smith and Young 2002), features like the Hawaiian Ridge are largely characterized by steep supercritical slopes and topography that occupy a significant fraction of the water column. For these cases, more complicated theories (Baines 1974, 1982; St. Laurent et al. 2003; Llewellyn Smith and Young 2003) or numerical modeling (Holloway and Merrifield 1999; Merrifield et al. 2001; Johnston and Merrifield 2003; Simmons et al. 2004) are required.

The Hawaiian Ridge is the site of the most intense surface tide loss per unit area in the global deep ocean (Egbert and Ray 2001; Simmons et al. 2004). Numerical modeling (Merrifield et al. 2001) and in situ measurements (Lee et al. 2006; Rudnick et al. 2003) find particularly intense internal tide energy fluxes radiating from French Frigate Shoals and Kaena Ridge in the Kauai Channel west of Oahu.

Few observations detail the structure of the deep-ocean internal tide where it is generated [for a review

Corresponding author address: Jonathan D. Nash, 104 COAS Admin Bldg. Oregon State University, Corvallis, OR 97331.
E-mail: nash@coas.oregonstate.edu

see Huthnance (1989)]. In the Bay of Biscay, Pingree and New (1989, 1991) found internal tide beams radiating from the continental shelf break. Holloway et al. (2001) found that the internal tide on the Australian northwest shelf is dominated by a vertically standing low mode that is dissipated close to its generation site. In Monterey Canyon, Petruncio et al. (1998) found that internal tides generated at the canyon mouth propagate either upcanyon or form horizontally standing modes, depending on the stratification. Kunze et al. (2002) computed baroclinic energy fluxes in the canyon and found them to be upcanyon and to decay onshore. At the Mendocino Escarpment, Althaus et al. (2003) found beams of energy radiating from the 1500-m-deep ridge; strong energy flux divergence characterized the generation site. In each of these studies, the observations were generally consistent with energy flow along internal tide characteristics, in accord with linear wave propagation. Highly nonlinear generation has also been observed in association with strong topographic flow over relatively shallow bathymetry (Chereskin 1983; Hibiya 1988; Loder et al. 1992; Farmer and Smith 1980) and from river plumes (Nash and Moum 2005).

In this paper, we describe the formation and structure of the internal tide across the southern half of Kaena Ridge (Fig. 1). Repeated full-depth profiles of velocity and density are used to examine the barotropic-to-baroclinic tidal conversion, the semidiurnal kinetic and potential energies, phase propagation, and energy flux. Low-vertical-wavenumber waves (modes 1–10) resolved by the sampling array carry most of the energy flux. Turbulent dissipation associated with higher vertical wavenumbers is presented by Klymak et al. (2006) and Lee et al. (2006).

This paper is organized as follows. In section 2, we describe the observations and analysis methods. The structure of the velocity and vertical displacements is described in section 3. In section 4, we present observations of the energetics. In section 5, we reconcile the generation and propagation pathways using two simple models. This is followed by conclusions in section 6.

2. Observations

During a spring tide in October 2000, a five-station section across Kaena Ridge was sampled from ridge crest (at about 1000-m depth) to the 3000-m isobath (Fig. 1). To obtain snapshots of the wave field that resolve the semidiurnal internal tide, stations 1–5 were sampled sequentially with expendable current profilers (XCPs; Sanford et al. 1993) for 21 h so that each station was occupied seven times with a 3-h repeat interval. Thirty-five XCPs were deployed with the ship under way, each returning baroclinic horizontal velocity (u, v) and temperature T with 2-m vertical and 4.5-km horizontal resolution.[1] Velocity profiles were made absolute using 30-min-averaged shipboard ADCP profiles (RD Instruments, 150 kHz; GPS referenced) over the upper 150 m.

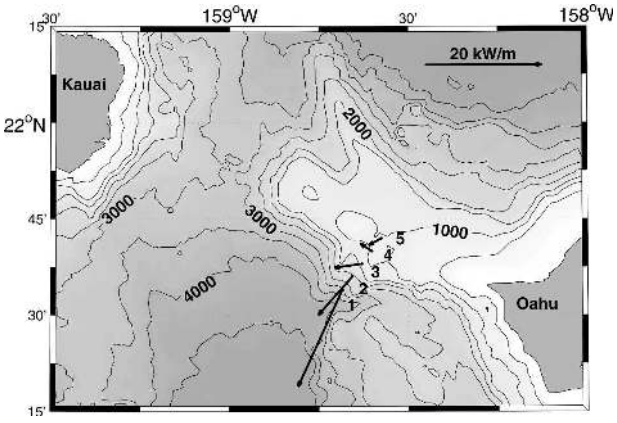

FIG. 1. Bathymetry of Kauai Channel (500-m contour intervals; bathymetry smoothed at 1 km) showing the five XCP stations (1–5) and AVP station (1) used in this study. The depth-integrated semidiurnal baroclinic energy flux computed from these observations is shown for reference.

At station 1, the 3000-m water depth exceeds the range of XCPs, so six full-depth profiles of u, v, T, salinity S, and microscale shear were collected using the absolute velocity profiler (AVP; Sanford et al. 1978, 1985) during the 15-h period immediately prior to the 21-h XCP surveys. AVP velocity profiles are collected during both descent and ascent, yielding 12 profiles of u and v. In the upper 2000 m, XCP and AVP data have statistically similar semidiurnal phase and amplitude of u, v, and T, allowing us to merge the data after applying a 24.8-h offset (i.e., Figs. 2e and 3e); XCP data from station 1 are not presented in this paper.

In the following we use a coordinate system aligned with the bathymetry (and our transect) so that *cross ridge* (x and u) is 37.4° east of north and *along ridge* (y and v) is 37.4° north of west.

Methods

The temporal evolution and spatial structure of the baroclinic perturbation fields of velocity, vertical displacement, and pressure ($\mathbf{u}'$, ξ, and p') are used to di-

[1] Roughly one-third of the XCP drops during this cruise were affected by pressure-induced thermistor failures over a segment of their depth range. This necessitated some interpolation over bad T data for this analysis.

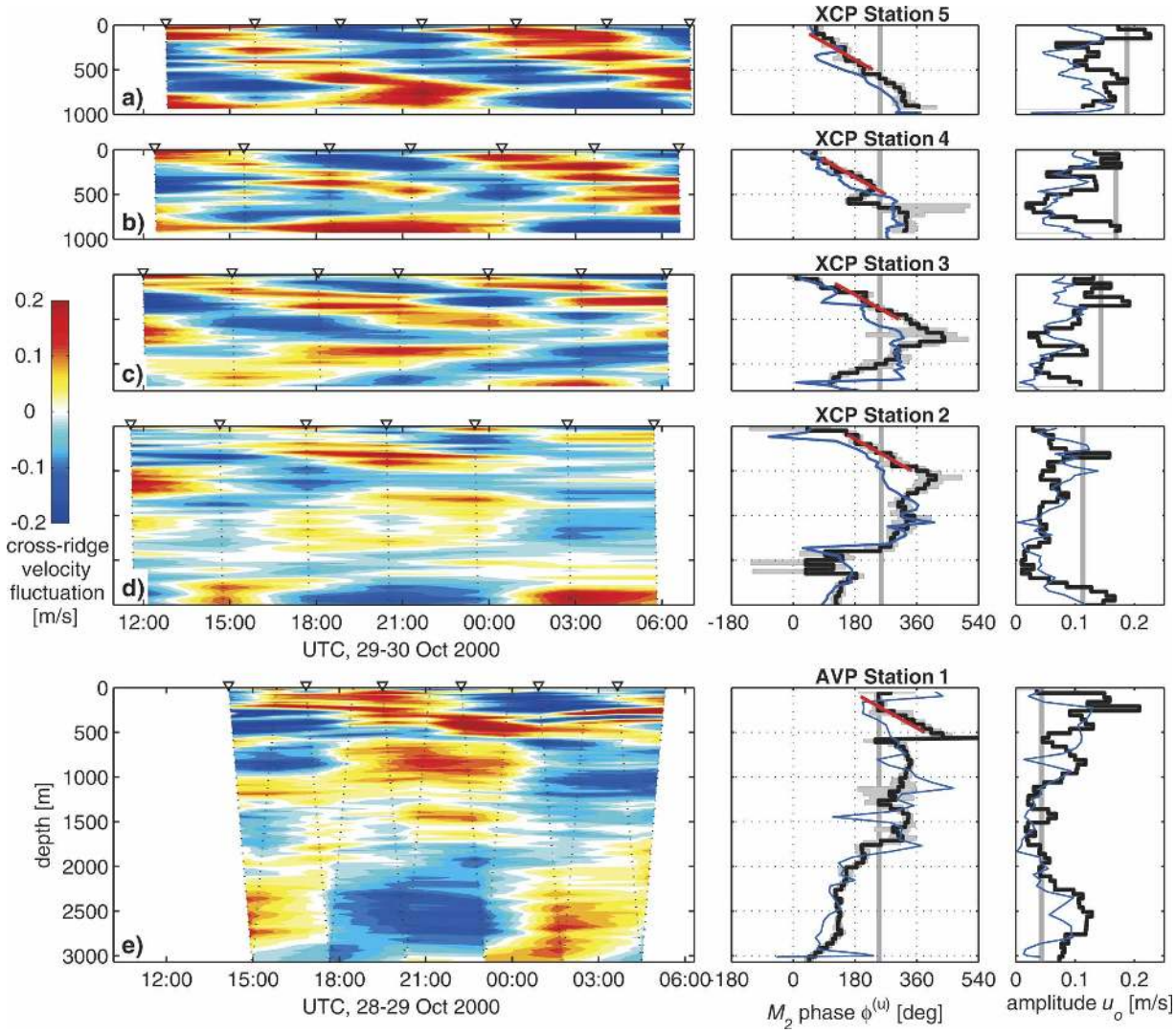

FIG. 2. Time series of upslope velocity fluctuation [$u' = u(z, t) - \bar{u}(z)$], semidiurnal phase $\phi^{(u)}$, and amplitude u_o at each station across Kaena Ridge, arranged from (a) on ridge to (e) farthest off ridge. (a)–(d) XCP stations in water depths <2000 m; (e) AVP data at station 1 obtained during the previous tidal cycle and offset by 24.8 h. Dotted lines in left-hand panels indicate profile locations; data contours are based on linear interpolation. Amplitude and phase were computed over 50-m intervals; 95% confidence limits on the baroclinic phase (gray shading) are indicated. Vertical gray lines indicate the phase and amplitude of the upslope barotropic velocity (derived from XCP or AVP data). Red lines represent least squares fits to semidiurnal phase between 100- and 500-m depths; blue lines represent the modeled output of Merrifield and Holloway (2002); see text.

agnose the dynamics of the semidiurnal internal wave field. From these, the energy flux $\mathbf{F}_E = \langle \mathbf{u}' p' \rangle$ is computed as the covariance of the wave-induced pressure p' and velocity $\mathbf{u}'$. By definition, p' and $\mathbf{u}'$ are baroclinic fluctuations, so have vanishing temporal and vertical averages. Our methods for computing these fluctuations, outlined below, follow Kunze et al. (2002), Althaus et al. (2003), and Nash et al. (2005).

Only temperature and horizontal velocity were measured by the XCPs. Four CTD profiles obtained before and after the XCP surveys had an unambiguous T–S relation and were used to infer S from T. To test its validity, the relationship was applied to the AVP T data, for which S was also measured but not used in the derived $S(T)$ relation. Based on this comparison, an rms error of 0.013 psu in S and 0.010 kg m^{-3} in potential density is associated with this approximation. Based on the mean stratification, this corresponds to errors in vertical displacement of $\xi_{\text{err}} = 12$ m at $z = 1000$ m and $\xi_{\text{err}} = 30$ m at $z = 1500$ m.

The density anomaly is estimated as $\rho'(z, t) = \rho(z, t) - \bar{\rho}(z)$, where $\rho(z, t)$ is the instantaneous density and

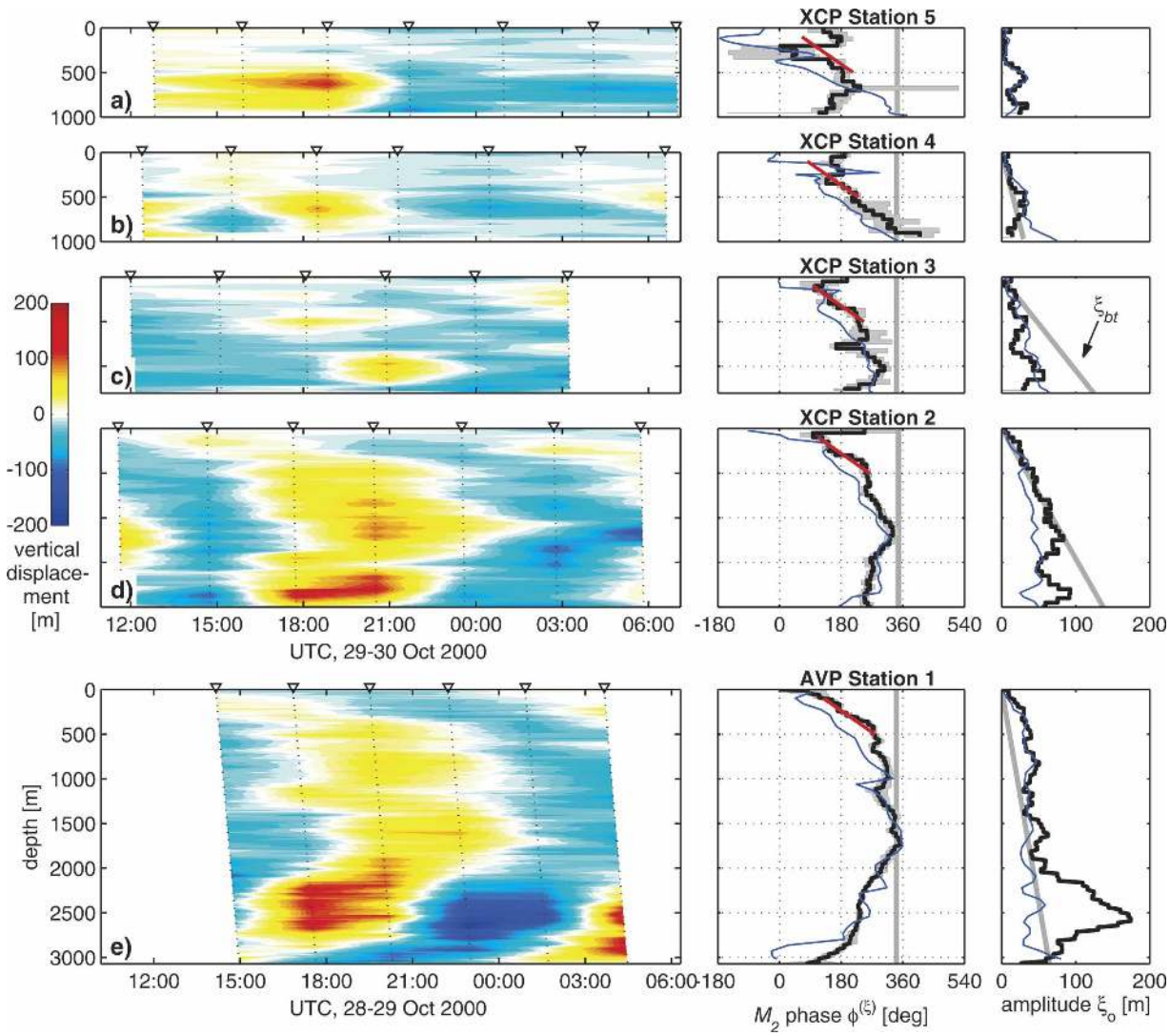

FIG. 3. As in Fig. 2, but for vertical displacement ξ, semidiurnal phase $\phi^{(\xi)}$, and amplitude ξ_o at five XCP stations across Kaena Ridge. Shading in middle panels represents 95% confidence limits on the baroclinic phase. Vertical gray lines in the right-hand panels indicate the phase and amplitude of vertical displacements induced by barotropic flow up a slope [ξ_{bt}; Eq. (7)].

$\overline{\rho}(z)$ is the time-mean vertical density profile, averaged over at least one wave period (>12.4 h). The pressure anomaly $p'(z, t)$ is calculated from the density anomaly using the hydrostatic equation,

$$p'(z, t) = p_{\text{surf}}(t) + \int_z^0 \rho'(\hat{z}, t) g \, d\hat{z}. \tag{1}$$

Although the baroclinic-induced surface pressure $p_{\text{surf}}(t)$ is not measured, it can be inferred from the baroclinicity condition that the depth-averaged pressure perturbation must vanish:

$$\frac{1}{H} \int_{-H}^0 p'(z, t) \, dz = 0. \tag{2}$$

The perturbation velocity is defined as

$$\mathbf{u}'(z, t) = \mathbf{u}(z, t) - \overline{\mathbf{u}}(z) - \overline{\mathbf{u}_o}(t), \tag{3}$$

where $\mathbf{u}(z, t)$ is the instantaneous velocity, $\overline{\mathbf{u}}(z)$ is its time mean, and $\overline{\mathbf{u}_o}(t)$ is determined by requiring baroclinicity:

$$\frac{1}{H} \int_{-H}^0 \mathbf{u}'(z, t) \, dz = 0. \tag{4}$$

Temporal averages $\overline{p}(z)$ and $\overline{\mathbf{u}}(z)$ represent station means over seven XCP occupations spanning ~18 h (or 6–12 AVP profiles spanning 15 h at station 1). These temporal averages were then used to determine the perturbation quantities following (1) and (3).

Profiles of isopycnal displacement, perturbation velocity and pressure are used to estimate the baroclinic energy flux $\mathbf{F}_E = \langle \mathbf{u}' p' \rangle$, baroclinic horizontal kinetic energy density HKE $= \langle u'^2 + v'^2 \rangle/2$, and available potential energy density APE $= N^2 \langle \xi^2 \rangle/2$. The angle brackets represent depth-dependent temporal averages, as computed from vertical profiles of semidiurnal amplitude and phase (described below).

Monte Carlo–type simulations are used to estimate how a broadband Garrett–Munk (GM) wave field alters results obtained from short-duration, discretely sampled time series. Following Nash et al. (2005), we generate an ensemble of 100 independent realizations of randomly phased, GM-contaminated wave fields with the observed semidiurnal energetics. Each realization is then sampled as were the observations; standard deviations may then be computed from the ensemble of these regenerated samplings. These error estimates account for broadband aliasing but do not account for aliasing by narrowband diurnal and near-inertial signals. Cospectral analysis of u and p' from a long, rapidly sampled time series (Rainville and Pinkel 2006) indicates that the semidiurnal waveband dominates the energy flux; diurnal fluctuations contribute to a lesser extent, accounting for ~15% of the total energy flux.

3. Structure of velocity and isopycnal displacement

Time series of perturbation velocity and vertical displacement constructed from individual XCP and AVP profiles are shown in Figs. 2 and 3. Stations 5 and 4 (Figs. 2a,b and 3a,b) represent observations on the ridge crest, while stations 3, 2, and 1 (Figs. 2c–e and 3c–e) are measurements over the steep ridge flank.

The overwhelming predominance of the semidiurnal signal in Kauai Channel (Levine and Boyd 2006; Rainville and Pinkel 2006) permits harmonic analysis to be applied to these short time series to extract tidal amplitudes and phase. We diagnose the semidiurnal velocity $u'(z) = u_o(z) \sin[\omega t - \phi^{(u)}(z)]$ by minimizing the residual $R(z)$ in a least squares sense to determine $A(z)$ and $B(z)$ in

$$u'(z) = A \cos(\omega t) + B \sin(\omega t) + R. \quad (5)$$

This yields the amplitude $u_o = (A^2 + B^2)^{1/2}$ and phase $\phi^{(u)} = -\arctan(A/B)$; $\omega = 2\pi/12.4$ h is the semidiurnal (M_2) frequency. Observations were obtained during spring tide, so short-duration fits contain contributions from all semidiurnal frequencies. Since energy scales with the square of amplitude, care must be taken in extending the energetics derived from these spring conditions to those at neap.

Amplitude and phase were computed over 50-m vertical intervals for each cross-ridge velocity, along-ridge velocity, vertical displacement, and pressure perturbation. The semidiurnal vertical velocity fluctuation w' was estimated from the fits as $d\xi/dt$. Semidiurnal fits capture roughly 70% of the variance of the cross-ridge perturbation velocity (i.e., $\overline{u_o^2} \approx 2.5\overline{R^2}$). Semidiurnal fits to $\xi(z, t)$ capture >90% of the isopycnal displacement variance off ridge (stations 1 and 2), but only 30% over the ridge crest (stations 4 and 5), where the signal is weak.

Time-averaged, subtidal currents $\overline{\mathbf{u}}(z)$ were strongest in the upper 700 m of the water column. These were predominantly southward (cross ridge), increasing from $|\overline{u}| < 0.05$ m s^{-1} over the ridge crest to $\overline{u} \sim -0.2$ m s^{-1} off ridge (stations 1 and 2). The along-ridge subtidal flow was significantly weaker $|\overline{v}| < 0.05$ m s^{-1}

a. Phase propagation of cross-ridge velocity

Raw time series of cross-ridge baroclinic velocity u' and its semidiurnal phase $\phi^{(u)}$ and amplitude u_o are shown in Fig. 2. The velocity is strongest and exhibits the simplest phase propagation at the shallowest stations, becoming progressively weaker and more complicated moving farther off ridge.

Semidiurnal barotropic velocity amplitudes were computed by applying harmonic analysis (5) to the depth-mean observations. The amplitude of the barotropic tide's cross-ridge velocity u_{bt}^o increases from 0.04 m s^{-1} at 3000 m to 0.19 m s^{-1} at the ridge crest (Fig. 2, thick vertical gray lines in rightmost panels). Barotropic velocity amplitudes exceed baroclinic over the ridge crest, while the reverse is true on the ridge flanks (station 1). Barotropic phase was estimated as $\phi_{bt}^{(u)} = 254 \pm 3°$, where $\pm$ represents variability between stations. In comparison, the phase of the barotropic tide from the TPX0.5 model (Egbert 1997) is $262 \pm 2°$, with amplitudes ranging from 0.05 m s^{-1} at station 1 to 0.18 m s^{-1} at station 5.

Over the ridge crest (stations 4 and 5; Figs. 2a,b), the semidiurnal phase propagation of upslope (cross ridge) velocity is downward and increases approximately linearly with depth, indicating upward energy propagation with a vertical wavelength of 1000 m. The semidiurnal amplitude is relatively constant with depth at ~0.16 m s^{-1}.

Over the steep slopes (stations 2 and 3; Figs. 2c,d), downward phase (upward energy) propagation is observed in the upper 600–700 m, similar to that over the ridge crest. This is mirrored by upward phase (downward energy) propagation below 700 m. Farthest off ridge (station 1, Fig. 2e), the phase structure becomes more complex. As with stations 2 and 3, downward (upward) phase propagation is observed in the upper (lower) part of the water column. However, there

are also hints of vertically standing behavior, with a roughly 180° phase shift between upper and lower water column velocities. The semidiurnal velocity amplitude u_o has significant vertical structure, exhibiting both surface and bottom intensification with range from 0.02 to 0.15 m s^{-1}.

In the upper 500 m, changes in phase are consistent between all five stations and approximately proportional to both depth z and horizontal distance from the ridge crest x (relative to station 5). The energy propagation is upward and off ridge. We illustrate this by performing a regression of $\phi^{(u)}$ with x and z (over all stations and between -500 m $< z < -100$ m), such that

$$\phi^{(u)} = \phi_o^{(u)} + \phi_x^{(u)}x + \phi_z^{(u)}z + R. \quad (6)$$

This linear fit is shown as the red lines in Fig. 2 and agrees well with the observations at each station. The coefficients have the values $\phi_o^{(u)} = 0 \pm 9°$, $\phi_x^{(u)} = 8.17 \pm 0.47°$ km^{-1}, and $\phi_z^{(u)} = 0.46 \pm 0.026°$ m^{-1}. These imply wavelengths $\lambda_z^{(u)} = 775 \pm 40$ m and $\lambda_x^{(u)} = 44 \pm 3$ km. This dominant horizontal wavelength (44 km) is roughly twice that of the horizontal spacing between the steep north and south flanks of Kaena Ridge (approximately 20–25 km, i.e., the width of the ridge crest; see Figs. 5 and 8). The ratio of vertical to horizontal wavelength in the upper 100–500 m is $\alpha = \lambda_z/\lambda_x = 0.017 \pm 0.002$, consistent with a single propagating semidiurnal wave in constant stratification, $\alpha = [(\omega^2 - f^2)/(N^2 - \omega^2)]^{1/2} = 0.019$, where $N^2 = 4.7 \times 10^{-5}$ s^{-2} represents the ridge-crest depth average.

b. Phase propagation of vertical displacement

In contrast to the baroclinic velocity, which is strongest and exhibits the clearest phase propagation over the ridge crest, vertical displacements are only significant over the steep flanks. There, the direction of phase propagation for ξ is qualitatively similar to that of u'—downward above 1000 m and upward below 1000 m. In section 5, we suggest that a superposition of at least two internal waves is needed to achieve symmetry over the ridge crest. One of the consequences of such a superposition is that vertical displacements are minimized over the ridge, as observed.

Since vertical displacements may be produced by barotropic flow over a sloping bottom, we also compute the barotropically induced vertical displacement (Baines 1982). For no normal flow at the bottom (defined by $z = -sx$), a barotropic tidal velocity $u_{\rm bt} = u_{\rm bt}^{\rm o} \sin(\omega t)$ induces a vertical velocity $w_{\rm bt}(z) = u_{\rm bt}s(z/H)$ throughout the water column. The associated vertical displacement $\xi_{\rm bt} = \int w_{\rm bt}\, dt$ is

$$\xi_{\rm bt} = \xi_{\rm bt}^{\rm o}(z/H)\sin(\omega t - \pi/2), \quad (7)$$

where $\xi_{\rm bt}^{\rm o} = u_{\rm bt}^{\rm o}s/\omega$ is the maximum vertical displacement. The bathymetry was low-pass filtered at 3 km (approximately the tidal excursion over the ridge crest) to compute the bottom slope s. Maximum vertical displacements occur 1/4 period after maximum upslope velocity, so the phase of this signal is $\phi_{\rm bt}^{(\xi)} = \phi_{\rm bt}^{(u)} + 90°$. These are indicated in Fig. 3. Note that $\xi_{\rm bt}$ is not removed from ξ so that ξ represents the total vertical displacement from both barotropic and baroclinic processes. Hence, ξ and p' may contain contributions associated with barotropic flow over a slope (i.e., $\xi_{\rm bt}$) and are hence not purely baroclinic.

Over the slope (stations 1 and 2), the observed vertical displacements are of similar amplitude to $\xi_{\rm bt}$. However, in the region of largest ξ (station 1, $z > 2000$ m), $\phi^{(\xi)}$ does not match $\phi_{\rm bt}^{(\xi)}$, but lags $\phi^{(u)}$ by ~90° (see Fig. 2). This suggests that those displacements are associated with a baroclinic wave, not the barotropic forcing. At station 3, the computed $\xi_{\rm bt}$ far exceeds the observed vertical displacements. Because the bottom slope changes rapidly at this station (see Fig. 6), this may indicate that our model of constant bottom slope is inappropriate for estimating $\xi_{\rm bt}$ near the slope break. This dissimilarity may also indicate that the observed displacements represent the baroclinic response, not barotropic heaving.

At stations 1–3, the phase of ξ propagates off ridge and downward in the upper 100–500 m, as observed with $\phi^{(u)}$. A linear regression,

$$\phi^{(\xi)} = \phi_o^{(\xi)} + \phi_x^{(\xi)}x + \phi_z^{(\xi)}z + R, \quad (8)$$

was performed at those stations to yield $\phi_o^{(\xi)} = 28 \pm 11°$, $\phi_x^{(\xi)} = 3.5 \pm 0.6°$ km^{-1}, and $\phi_z^{(\xi)} = 0.37 \pm 0.02°$ m^{-1}. Stations 4 and 5 were omitted because the amplitudes of ξ are weak, so its phase is poorly defined. The regression coefficients imply a propagating wave with wavelength $\lambda_z^{(\xi)} = 970 \pm 50$ m, $\lambda_x^{(\xi)} = 103 \pm 20$ km, and $\alpha = 0.008 \pm 0.002$, about one-half of that predicted by linear theory. While the λ_z estimates from u' and ξ are consistent with each other, $\lambda_x^{(\xi)}$ and $\lambda_x^{(u)}$ differ by a factor of 2. As a result, $\phi^{(\xi)}$ is in quadrature with $\phi^{(u)}$ at station 1 (suggestive of a propagating internal wave) but approximately in phase at station 5. The differences between $\lambda_x^{(u)}$ and $\lambda_x^{(\xi)}$ cannot be explained by interference between horizontally opposing waves over the ridge crest for which both wavelengths are equal (see section 5). It may also be attributed to experimental error in computing $\phi_x^{(\xi)}$, as $\lambda_x^{(\xi)}$ was computed from only three stations (one of which was occupied on the previous tidal cycle) and in a region with relatively weak vertical displacements (i.e., $\xi_o < 50$ m).

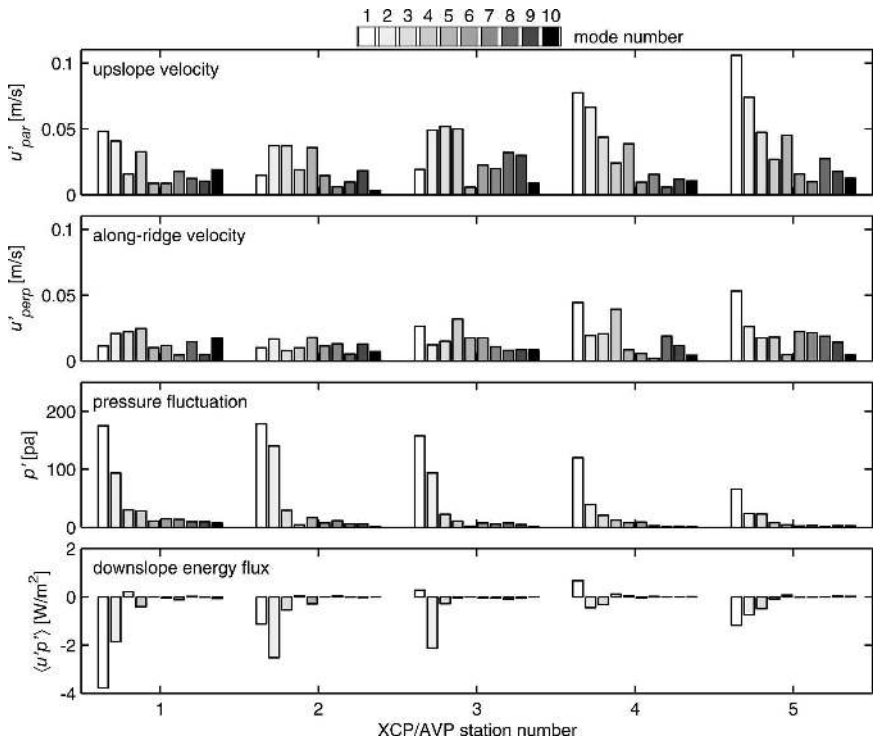

FIG. 4. Modal decomposition of velocity, pressure, and energy flux as a function of distance across Kaena Ridge. These modal amplitudes represent the projection of semidiurnal fits to u', v', and p' onto the first 10 flat-bottom vertical modes at each station; $\langle u'p' \rangle$ is the product of the amplitudes of u', p', and the cosine of the difference in their phases. Because of changes in the water depth, the dimensional wavelengths associated with mode one over the ridge are similar to mode 2 off ridge. Modal structure functions are normalized to unity variance, so modal amplitudes are representative of depth averages not depth integrals. Depth-integrated energy fluxes (the sum of the modal amplitudes of $\langle u'p' \rangle$, multiplied by the water depth) are shown in Fig. 5.

c. Model comparisons

We compare our observations with the model results of Merrifield and Holloway (2002). There is qualitative agreement between the observed and modeled velocity and vertical displacement (right-hand panels of Figs. 2 and 3). Both model and observations indicate an approximate linear increase in phase with depth at the ridge crest (stations 5 and 4; Figs. 2a,b and 3a,b). Farther from the ridge, the bifurcation in phase propagation (station 3; Figs. 2c and 3c) is less apparent in the model than the observations. The most notable disagreement occurs for vertical displacement at station 1 for which the observations at 2500 m are roughly 3 times those modeled.

We emphasize that the scale on each phase plot (720°) highlights gross similarities but conceals differences. Closer scrutiny of Figs. 2 and 3 indicates that differences in phase between model and observations may exceed 90°. Nevertheless, most vertical trends (and many of the smaller features) are similar in the model and observations. This is noteworthy, considering that the model represents a simplified deterministic process and our observations represent not much more than a single tidal cycle.

d. Modal content

The barotropic plus first 10 flat-bottom baroclinic modes were computed using the stratification at each station. Semidiurnal harmonic fits were projected onto these modes to determine the dominant vertical scales of u', v', p', and $\langle u'p' \rangle$ (Fig. 4). Over the ridge (stations 4 and 5), the up-ridge and along-ridge velocities (u', v') are strong and dominated by the lowest modes, while the pressure fluctuations are comparatively weak. In contrast, pressure fluctuations over the slope are strong (stations 1 and 2), despite weak velocities. The correlation $\langle u'p' \rangle$ is much stronger over the slope than over the ridge. Only on the flank (station 1) does mode 1 dominate the energy flux, with almost all being carried in modes 1 and 2. Lee et al. (2006) find similar

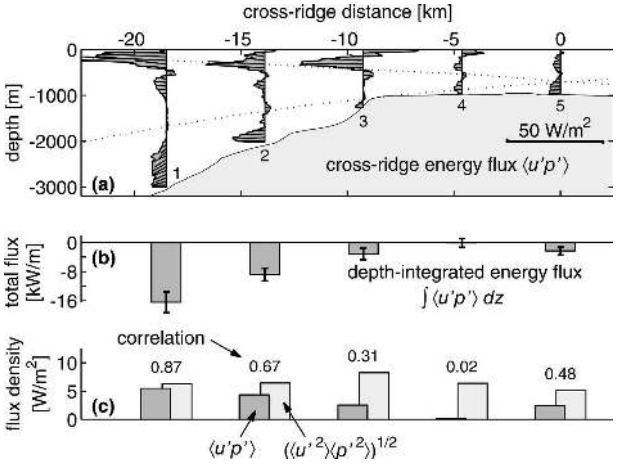

FIG. 5. Cross-ridge distribution of the upslope (cross ridge) component of (a) energy flux, (b) depth-integrated energy flux with standard error, and (c) coherence between u' and p'. Black vectors in (a) represent the vertical and horizontal components of the energy flux ($\langle u'p' \rangle$, $\langle w'p' \rangle$); the vertical component has been stretched commensurate with the figure's vertical exaggeration. Two internal tide ray paths originating from critical topography are indicated with dashed lines. In (c), the absolute value of the depth-averaged energy flux density $\overline{\langle u'p' \rangle}$ (dark shading) is compared to the square root of the product of variances $(\overline{\langle u'^2 \rangle}\,\overline{\langle p'^2 \rangle})^{1/2}$ (light shading), where the overbar represents a vertical average; the indicated coherence represents the ratio of these two quantities.

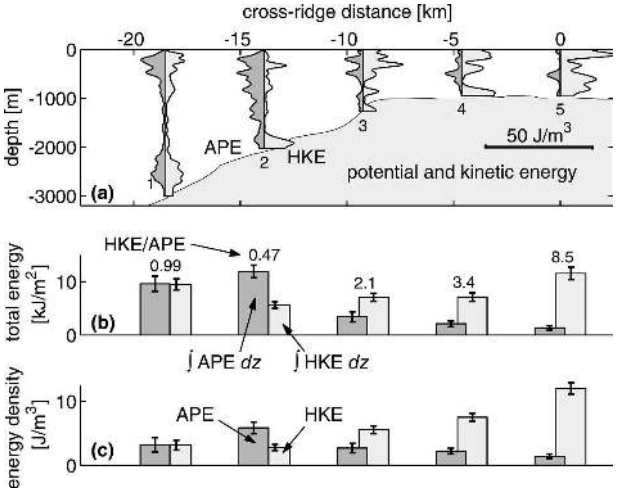

FIG. 6. Cross-ridge distribution of (a) available potential energy density (APE, dark shading) and horizontal kinetic energy density (HKE, light shading) in the semidiurnal waveband. (b) The depth-integrated kinetic and potential energies and their ratios (numbers). (c) The associated energy densities. Error bars represent Monte Carlo–derived standard deviations.

modal distributions at all of the 3000-m-isobath stations.

4. Energetics

In the following, we examine the structure of the horizontal and vertical energy flux, as well as the kinetic and potential energy. Each are derived from semidiurnal harmonic fits to perturbation quantities (u', v', ξ, and p'), as discussed in sections 2 and 3. Errors represent standard deviations computed from 100 randomly phased, GM-contaminated synthetic time series with energetics and sampling consistent with the observations (Nash et al. 2005).

a. Energy flux

The cross-ridge and vertical components of the semidiurnal energy flux ($\langle u'p' \rangle$, $\langle w'p' \rangle$) are shown in Fig. 5. Over the ridge (stations 4 and 5) the energy-flux density and its depth average are small. The depth-integrated flux increases monotonically over the slope (stations 1–3), where it forms two distinct beams:

- in the upper 500 m, where the energy flux is off ridge and upward;
- in the lower 1000 m, where the energy flux is off ridge and downward.

These are also the two regions where the phase of u' and ξ is well defined and in quadrature (see Figs. 2 and 3). In the upper (lower) beam, phase propagation was downward (upward) and off ridge, consistent with the vector direction and spatial distribution of the energy flux. Month-long time series acquired from R/P *Floating Instrument Platform* (*FLIP*) (Rainville and Pinkel 2006) capture the initial manifestation of the upper beam, with ~6 W m^{-2} emerging in the upper water column near XCP station 4.

Despite the product of variances of u' and p' being of similar magnitude at each station (Fig. 5c, light gray), the in-phase coherence,

$$\mathrm{coh} = \frac{\overline{\langle u'p' \rangle}}{(\overline{\langle u'^2 \rangle}\,\overline{\langle p'^2 \rangle})^{1/2}}, \tag{9}$$

indicates that these fluctuations do not participate in forming a net flux over the ridge. Here u' and p' become progressively more coherent moving off ridge and ultimately become 90% coherent at station 1, at which point most of the semidiurnal velocity and pressure fluctuations contribute to the energy flux.

b. Energy

Horizontal kinetic energy HKE, available potential energy APE, and their depth integrals are shown in Fig. 6. The energy density is dominated by HKE over the

ridge and by APE over the slope, with the ratio in HKE/APE varying by more than an order of magnitude. This structure contrasts the expected value for a single propagating wave for which HKE/APE is an intrinsic property equal to $(\omega^2 + f^2)/(\omega^2 - f^2) = 1.34$ for M_2 at 21.6°N.

Only at the farthest off-ridge station does HKE/APE approach its expected value for a freely propagating wave. This is also the only station where APE and HKE have similar vertical structure.

c. Ridge-top energetics

The near-constant horizontal and vertical phase propagation that spans the ridge crest and slope [i.e., (6) and Fig. 2] suggests that the south-going near-surface beam (Fig. 5) originates on the opposite (north) side of the crest. In addition, the total semidiurnal energy density (APE + HKE, Figs. 4 and 6c) is highest over the ridge crest despite the vanishing energy flux there (Fig. 5).

Because of the symmetry of the ridge, at least two waves with opposing horizontal group velocity are required to explain the ridge-crest energetics. Given the observed energy density and zero net energy flux, we seek a ridge-crest estimate for the energy flux associated with just the north- or southbound wave. Along-ridge contributions to the energy density are neglected. Based on a modal decomposition, the energy flux may be represented as a product of the nth vertical mode energy $E^{(n)}$ and its group velocity $c_g^{(n)}$ so that the total flux in the first 10 modes is

$$\langle u'p' \rangle_{\text{est}} = \sum_{n=1}^{10} c_g^{(n)} E^{(n)}. \tag{10}$$

Using the observed modal decomposition (Fig. 4), we find the total depth-integrated energy flux $\int \langle u'p' \rangle_{\text{est}}\, dz$ at stations 4 and 5 to be 9.7 and 11.5 kW m^{-1}, respectively; 90%–95% of the flux is carried by the first three modes. This represents the sum of energy flux magnitudes, with contributions from both north- and southbound internal tides. Since the net energy flux (vector sum) over the ridge crest is negligible, we attribute one-half of $\int \langle u'p' \rangle_{\text{est}}\, dz$ = 9.7–11.5 kW m^{-1} (i.e., 5–6 kW m^{-1}) to each of the north- and southbound waves. This is similar to the ~4 kW m^{-1} observed in the upward-propagating beam at station 3 (Fig. 5). In comparison with the 16 kW m^{-1} that ultimately emerges from the ridge, this estimate suggests that roughly one-third of the off-ridge energy flux originates from the opposite flank.

5. Interpretation

a. Generation

Following Baines (1982), the total rate of work by barotropic tidal currents interacting with topography is the product of the Baines (1982) force $F_b = N^2 w_{\text{bt}} \omega^{-1}$ and the barotropically induced vertical velocity, $w_{\text{bt}} = \mathbf{u}_{\text{bt}} \cdot \nabla \mathbf{H}(z/H)$:

$$F_b w_{\text{bt}} = \frac{N^2 w_{\text{bt}}^2}{\omega} = \frac{N^2 [\mathbf{u}_{\text{bt}} \cdot \nabla \mathbf{H}(z/H)]^2}{\omega}, \tag{11}$$

which varies in time as $\sin^2(\omega t)$. If all of this power entered the internal wave field, the depth-integrated energy flux over the region of generation (between x_1 and x_2) would be

$$\Delta F_E = \int_{x_1}^{x_2} \left[\int_{-H(x')}^{0} \langle F_b w_{\text{bt}} \rangle\, dz \right] dx', \tag{12}$$

where $\langle \ldots \rangle$ represents a time average and dissipation is neglected.

A comparison between (12) and the numerical simulations of Khatiwala (2003) indicates that ΔF_E represents an upper bound on internal tide generation. For a ridge width of similar scale to the mode-1 horizontal wavelength, as over Kaena Ridge, Khatiwala's numerical results agree with (12) to within 10%. However, (12) overpredicts the energy flux in the limits of both longer and shorter wavelength topography. For long-wavelength topography, the horizontal scale of $\langle F_b w_{\text{bt}} \rangle$ exceeds that of the lowest vertical mode so that much of the transfer remains as part of the barotropic flow. For short-wavelength topography, Baines (1982) overpredicts the induced vertical velocity because of blocking, yielding infinite w_{bt}, $\langle F_b w_{\text{bt}} \rangle$ and ΔF_E in the limit of a knife edge.

Integration of (12) over Kaena Ridge yields $\Delta F_E(x)$ ~ 25 kW m^{-1} per side, as shown in Fig. 7 (top). This exceeds observed $\langle u'p' \rangle$ by ~30%–50%, so is consistent with ΔF_E as an upper bound for generation, even after turbulent dissipation is taken into consideration as an energy sink ($\int \rho \epsilon\, dx\, dz \simeq 1.2$ kW m^{-1} for each side of Kaena Ridge; Klymak et al. 2006).

For Kaena Ridge (Fig. 7), barotropic power $F_b w_{\text{bt}}$ is evenly distributed below 300 m—a result of the compensation of the decay of w_{bt}^2 away from the bottom by the vertical structure of N^2. For a two-dimensional ridge, energy may radiate along one of four internal tide characteristics, given by $dz/dx = \pm\alpha = \pm[(\omega^2 - f^2)/(N^2 - \omega^2)]^{1/2}$. The pathways for energy flow can be determined by assuming that energy refracts by stratification and reflects from the surface and boundaries according to linear theory (Eriksen 1982). At Kaena

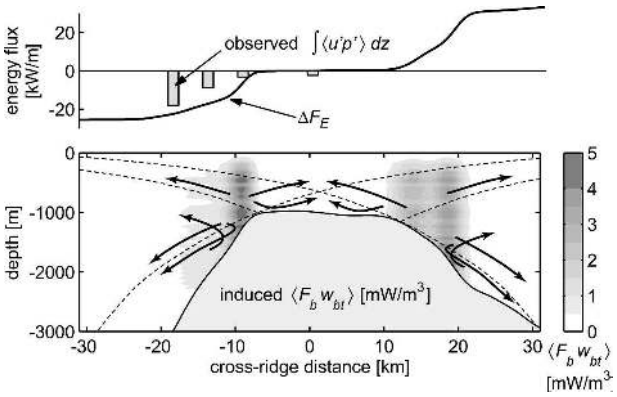

FIG. 7. (bottom) Distribution of the time-average power associated with barotropic flow over Kaena Ridge (11) using TPX0.5 barotropic currents and 3-km smoothed bathymetry. Arrows indicate pathways for energy flow along internal tide ray paths. Internal tide characteristics emanating from critical bathymetry (dotted lines) are indicated and divide the dynamical regions. (top) An upper bound to the depth-integrated energy flux is calculated by assuming ridge symmetry and integrating (12) from 0 to x.

Ridge, downward propagation is expected off ridge from the deep supercritical flanks. However, the broad subcritical ridge top leads to the predominance of upward energy propagation in the upper water column (Fig. 7). This is consistent with the observed phase structure of u' in Figs. 2a and 2b and the intense HKE over the ridge crest. Off ridge, the energy pathways are corroborated by the observed vector energy flux (Fig. 5).

b. The ridge crest as a horizontally standing mode

Barotropic flow over Kaena Ridge simultaneously generates upward $\xi_{\rm bt}$ at $x \sim -10$ km and downward $\xi_{\rm bt}$ at $x \sim 15$ km. Assuming these displacements drive a baroclinic wave spanning the ridge crest, the 25-km separation implies a wave with $\lambda_x = 50$ km. From the dispersion relation, this implies $\lambda_z = 850$ m, similar to that observed in sections 3a and 3b. This suggests that the internal tide's vertical wavelength over the ridge crest may be set by the width of the ridge (i.e., the separation between generation regions).

Over the ridge crest (stations 5 and 4; Figs. 2a,b), a linear regression of $\phi^{(u)}$ with depth suggests $\lambda_z = 1000$ m; the average amplitude is 0.16 m s^{-1}.[2] We model this velocity structure as a superposition of two linear waves with amplitude $u_o = 0.08$ m s^{-1} and vertical wavelength $m = -2\pi/1000$ m (downward phase propagation) in constant stratification. They have opposite horizontal wavenumbers $k = \pm\alpha m$, so that one propagates north and the other south, and are phased so that the resultant wave field is symmetric about $x = 0$. The horizontal energy flux density associated with each is 4.2 W m^{-2}, yielding a depth integral of 4.2 kW m^{-1}—about 30% less than that estimated from (10) because only one wavelength is considered here. Neither surface nor bottom boundary conditions can be satisfied by this formulation. However, the resultant cross-ridge standing mode satisfies our above intuition that $\xi_{\rm bt}$ is 180° out of phase in the opposing generation regions (separated horizontally by 25 km).

The time-averaged APE, HKE, and energy flux for this superposition are

$$\begin{aligned}
\text{APE} &= \frac{u_o^2 N^2 \alpha^2}{\omega^2}\sin^2(kx),\\
\text{HKE} &= u_o^2\cos^2(kx)\left(1+\frac{f^2}{\omega^2}\right),\\
\langle u_{\rm tot}p_{\rm tot}\rangle &= 0,\\
\langle v_{\rm tot}p_{\rm tot}\rangle &= \frac{\rho_o f u_o^2}{k\omega^2}(\omega^2-f^2)\sin(2kx), \quad \text{and}\\
\langle w_{\rm tot}p_{\rm tot}\rangle &= \frac{2\rho_o u_o^2}{m\omega}(\omega^2-f^2)\sin^2(kx). \qquad (13)
\end{aligned}$$

The horizontal structure of these is shown in Fig. 8. Spatial periodicity arises because the two superimposed waves are phase locked and produce bands of interference. Unlike a mode that is standing in both vertical and horizontal directions (i.e., Petruncio et al. 1998), there is no depth dependence in any of these averages because vertical propagation has been retained.

Maxima in APE and $\langle w'p'\rangle$ occur at $x = (2n-1)\pi/(2k)$; HKE is out of phase with maxima at $x = n\pi/k$ (Fig. 8b). As compared with a single propagating wave for which HKE/APE $= (\omega^2+f^2)/(\omega^2-f^2) = 1.34$ uniformly, the ratio HKE/APE for this vertically propagating, horizontally standing mode ranges from ∞ over the ridge crest to 0 at $x = \pm\lambda_x/2$. Note that the transverse energy flux $\langle v'p'\rangle_{\rm tot}$ does not vanish, having extrema at 14-km intervals. This is consistent with the westward component of the observed energy flux at stations 3 and 4 (Fig. 1).

We stress that the standing wave pattern (13) is plausible only where both north- and southbound waves are present (i.e., between the two generation regions—over the ridge crest). In this region, the comparison in Fig. 8 suggests wave interference as a means for generating the observed HKE/APE structure. HKE density is maximum over the ridge crest in both model and observations, with values of 7 and 8–11 J m^{-3}, respectively. APE increases over the slope to ~6 J m^{-3} at

[2] For stations 4 and 5, $\lambda_z \sim 1000$ m is slightly larger than that determined when all stations are used in the regression (6).

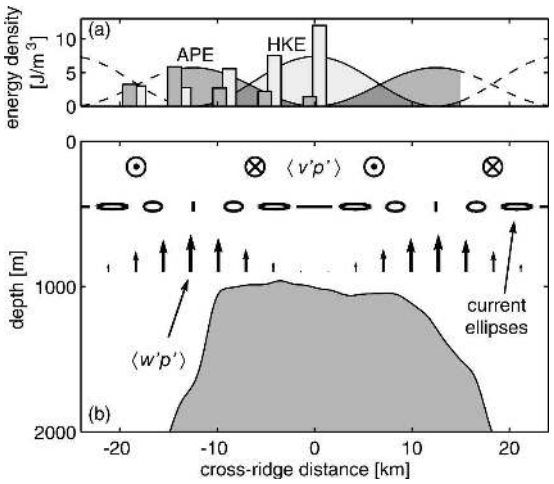

FIG. 8. The structure of an internal tide formed from the superposition of two plane waves: one propagating toward $+x$, $+z$ and the other toward $-x$, $+z$. Each wave has 1000-m vertical wavelength, as observed over the ridge crest (the associated horizontal wavelength $\lambda_x = 56$ km). Average APE (dark shading) and HKE (light shading) are shown by smooth curves in (a); curves are dashed where a two-wave superposition is not valid ($|x| > 15$). Bars in (a) indicate the observed energy densities shown in Fig. 6c. The resultant current ellipses are shown in (b); vertical exaggeration of current ellipses is consistent with the figure aspect ratio. Arrows represent the distribution of vertical energy flux, and the along-ridge energy flux is indicated with $\otimes$ (into the page) and $\odot$ (out of the page). All energetics are independent of depth and periodic across the ridge with period $\lambda_x/2$ except for the cross-ridge energy flux, $\langle u'p' \rangle$, which is zero everywhere.

$x = 14$ km in both observations and model. The model is not applicable seaward of the generation region ($x \sim -14$ km), where most of the wave flux is off ridge (Fig. 5).

Regions of high APE and $\langle w'p' \rangle$ coincide with the steep ridge flanks where ξ_{bt} and $\langle F_b w_{bt} \rangle$ are largest (Fig. 7). In contrast, the superposition produces weak vertical displacements and APE over the relatively flat ridge crest. We hypothesize that it is no coincidence that the dominant vertical wavelength over Kaena Ridge is 1000 m, as this is the required wavelength to create HKE/APE banding that matches the ~25 km horizontal spacing between generation regions. It therefore appears that the vertical and horizontal wavelengths of the internal tide ($\lambda_z \sim 1000$ m and $\lambda_x \sim 50$ km) are tuned to the topography.

6. Conclusions

Phase propagation, energy density, and energy flux $\langle u'p' \rangle$ of the semidiurnal internal tide have been examined at Kaena Ridge during a spring tide in October 2000. Over the ridge crest, u' and p' are out of phase and yield negligible net depth-integrated energy flux. Over the steep slopes of the ridge flank, the energy flux diverges strongly, forming two beams radiating to the south: one propagates downward near the flank bottom, the other upward near the surface. In these beams, u' and p' are in phase, with 90% of the fluctuations contributing to the ~16 kW m^{-1} depth-integrated energy flux carried past the 3000-m isobath.

The beam near the flank bottom occurs below a semidiurnal internal wave characteristic emanating from the rim of the ridge crest. According to linear theory, ridge-crest energy cannot penetrate into this region, so the source of this beam must be the nearby steep, supercritical slope. In contrast, phase propagation in the upper 500 m is continuous across the ridge, suggesting that both northern and southern flanks influence the upward-propagating beams. Based on the phase propagation of velocity, the vertical and horizontal wavelengths are 800 m and 44 km, respectively (the corresponding wavelengths based on ξ are 1000 m and 100 km). The source of the discrepancy between $\lambda_x^{(u)}$ and $\lambda_x^{(\xi)}$ has yet to be rationalized but may arise because ξ represents total vertical displacement, not just the baroclinic response.

APE and HKE vary dramatically across the ridge. The highest APE occurs over the steep slopes, whereas the highest HKE occurs over the crest. As a result, the energy ratio HKE/APE varies by more than a factor of 10 across the ridge and only attains the intrinsic value for a freely propagating wave (1.34) at the farthest off-ridge station (Fig. 6).

Because there is no net energy flux over the ridge crest, it is tempting to assume that the wave field emerging from the ridge is generated at the nearest flank. However, the intense ridge-crest HKE indicates that this is not the case and that the wave field has multiple sources. While the three-dimensionality of the ridge adds complexity and produces along-ridge propagation (Rainville and Pinkel 2006), we employ a two-dimensional approach to explain the cross-ridge energy and energy-flux structure. Assuming a symmetric superposition of north- and southbound waves over the ridge crest, each must carry ~5–6 kW m^{-1} to account for the modal distribution of energy density (10); inclusion of along-ridge contributions to the energy density would reduce this estimate. Based on linear theory, such a superposition leads to a horizontally standing mode (Nash et al. 2004) with alternating bands of HKE and APE. The spacing between bands is set solely by the wavenumber of the internal tide. We find that the magnitude and expected spacing between bands of maximum HKE and APE (~14 km) are consistent with that observed.

Barotropic flow over Kaena Ridge simultaneously

displaces isopycnals in opposite directions over either ridge flank. The ~25 km horizontal spacing between generation regions (Fig. 7) sets a horizontal scale of the forcing to generate waves with horizontal wavelength λ_x ~50 km. Through the dispersion relation, this implies a vertical wavelength of λ_z ~1000 m, as observed.

We thus suggest that the vertical wavelength of baroclinic response is set by the horizontal scale of the feature that generates it. For Kaena Ridge, this wavelength is 1000 m, similar to the water depth. We speculate that Kaena Ridge is a particularly efficient generation site for the semidiurnal internal tide because of this agreement. A much narrower feature may generate a higher wavenumber response and, conversely, a wider feature may generate lower vertical wavenumbers. Since high wavenumbers dissipate more quickly than the low modes (St. Laurent and Nash 2004), the ridge width (which presumably sets the near-field wavenumber content) may be the important parameter in determining the fraction of energy that is dissipated locally as compared with the fraction that is radiated away.

Determination of the barotropic-to-baroclinic conversion rate from steep, large-amplitude topography has had recent theoretical success for knife-edge and top-hat bathymetries (Llewellyn Smith and Young 2003; St. Laurent et al. 2003). For Hawaiian Ridge geometry, these predict energy fluxes of appropriate magnitude and an energy-flux spectrum in agreement with observations (St. Laurent and Nash 2004). A common feature of the solutions is the beamlike character of the baroclinic response, similar to that observed. For example, in the case of the top-hat ridge (St. Laurent et al. 2003), beams emanate from ridge discontinuities along ray paths. These beams form a superposition of mostly upward-propagating energy over the ridge crest, and upward- and downward-propagating waves away from the ridge. Significant baroclinic energy occurs over the ridge top despite zero net energy flux there. However, the vertical wavenumbers generated by top-hat topography depend primarily on the ridge height ($\delta = h_o/H$) and only very weakly on the ridge width (L. St. Laurent 2005, personal communication) Such steep-topography models therefore do not predict that the ridge-top vertical wavelength is set by the ridge width.

The power available from the barotropic tide (Baines 1982; $\langle F_b w_{\mathrm{bt}} \rangle$) represents an upper bound for baroclinic generation. Comparisons with Khatiwala (2003) indicate that it fails in the limits of large- and small-wavelength topography. For Kaena Ridge, it overpredicts the energy flux by 30%–50%.

Klymak et al. (2006) find 1.1–1.3 kW m^{-1} of turbulent dissipation integrated over the cross-ridge section considered here, amounting to ~10% of the total flux observed. Klymak et al. (2006) and Levine and Boyd (2006) provide evidence for enhanced mixing over and on the upper flanks of Kaena Ridge, sites with near-critical slopes where linear theory predicts a high wavenumber response and associated wave dissipation.

These observations produce as many questions as answers. For example, what is the fate of baroclinic tidal beams as they reflect from the bottom and highly stratified upper ocean? Does the ridge width set the energy partitioning between high and low wavenumbers? Are high modes simply dissipated, or do they undergo other internal wave transformations? And, most important, does the radiated energy ultimately dissipate in the appropriate locations and with a sufficient mixing efficiency to contribute significantly to global mixing budgets?

Acknowledgments. The authors thank John Dunlap, Art Bartlett, Bob Drever, Eric Boget, Dicky Allison, Alana Althaus, and the captain and crew of the R/V *Wecoma* for making these measurements possible. Princeton Ocean Model output was kindly provided by Mark Merrifield. Lou St. Laurent shared his code to determine top-hat generation. We thank Luc Rainville and Chris Garrett for their helpful reviews of this manuscript. This research was funded under NSF Grants OCE-98-19537 and OCE-01-36116.

REFERENCES

Alford, M. H., 2003: Energy available for ocean mixing redistributed by long-range propagation of internal waves. *Nature,* **423,** 159–162.

Althaus, A. M., E. Kunze, and T. B. Sanford, 2003: Internal tide radiation from Mendicino Escarpment. *J. Phys. Oceanogr.,* **33,** 1510–1527.

Baines, P. G., 1974: The generation of internal tides over steep continental slopes. *Proc. Roy. Soc. London,* **277A,** 27–58.

——, 1982: On internal tide generation models. *Deep-Sea Res.,* **29,** 307–338.

Bell, T. H., 1975: Topographically generated internal waves in the open ocean. *J. Geophys. Res.,* **80,** 320–327.

Chereskin, T. K., 1983: Generation of internal waves in Massachusetts Bay. *J. Geophys. Res.,* **88,** 2649–2661.

Egbert, G. D., 1997: Tidal data inversion: Interpolation and inference. *Progress in Oceanography,* Vol. 40, Pergamon, 81–108.

——, and R. D. Ray, 2001: Estimates of M2 tidal energy dissipation from TOPEX/Poseidon altimeter data. *J. Geophys. Res.,* **106,** 22 475–22 502.

Eriksen, C. C., 1982: Observations of internal wave reflection off sloping bottoms. *J. Geophys. Res.,* **87,** 525–538.

Farmer, D. M., and J. D. Smith, 1980: Tidal interaction of stratified flow with a sill in Knight Inlet. *Deep-Sea Res.,* **27A,** 239–254.

Hibiya, T., 1988: The generation of internal waves by tidal flow over Stellwagen Bank. *J. Geophys. Res.,* **93,** 533–542.

Holloway, P. E., and M. A. Merrifield, 1999: Internal tide genera-

tion by seamounts, ridges and islands. *J. Geophys. Res.,* **104,** 25 937–25 951.

——, P. G. Chatwin, and P. Craig, 2001: Internal tide observations from the Australian North West Shelf in summer 1995. *J. Phys. Oceanogr.,* **31,** 1182–1199.

Huthnance, J. M., 1989: Internal tides and waves near the continental shelf edge. *Geophys. Astrophys. Fluid Dyn.,* **48,** 81–105.

Johnston, T. M. S., and M. Merrifield, 2003: Internal tide scattering at seamounts, ridges and islands. *J. Geophys. Res.,* **108,** 3180, doi:10.1029/2002JC001528.

Kantha, L. H., and C. C. Tierney, 1997: Global baroclinic tides. *Progress in Oceanography,* Vol. 40, Pergamon, 163–178.

Khatiwala, S., 2003: Generation of internal tides in an ocean of finite depth: Analytical and numerical calculations. *Deep-Sea Res.,* **50,** 3–21.

Klymak, J. M., and Coauthors, 2006: An estimate of tidal energy lost to turbulence at the Hawaiian Ridge. *J. Phys. Oceanogr.,* **36,** 1148–1164.

Kunze, E. L., L. K. Rosenfeld, G. S. Carter, and M. C. Gregg, 2002: Internal waves in Monterey Submarine Canyon. *J. Phys. Oceanogr.,* **32,** 1890–1913.

Lee, C. M., E. Kunze, T. B. Sanford, J. D. Nash, M. A. Merrifield, and P. E. Holloway, 2006: Internal tides and turbulence along the 3000-m isobath of the Hawaiian Ridge. *J. Phys. Oceanogr.,* **36,** 1165–1183.

Levine, M. D., and T. J. Boyd, 2006: Tidally forced internal waves and overturns observed on a slope: Results from HOME . *J. Phys. Oceanogr.,* **36,** 1184–1201.

Llewellyn Smith, S. G., and W. R. Young, 2002: Conversion of the barotropic tide. *J. Phys. Oceanogr.,* **32,** 1554–1566.

——, and ——, 2003: Tidal conversion at a very steep ridge. *J. Fluid Mech.,* **495,** 175–191.

Loder, J. W., D. Brickman, and E. P. W. Home, 1992: Detailed structure of currents and hydrography on the northern side of Georges Bank. *J. Geophys. Res.,* **97,** 14 331–14 351.

Merrifield, M. A., and P. E. Holloway, 2002: Model estimates of M2 internal tide energetics at the Hawaiian Ridge. *J. Geophys. Res.,* **107,** 3179, doi:10.1029/2001JC000996.

——, ——, and T. M. S. Johnston, 2001: Internal tide generation at the Hawaiian Ridge. *Geophys. Res. Lett.,* **28,** 559–562.

Munk, W., and C. Wunsch, 1998: Abyssal recipes II: Energetics of tidal and wind mixing. *Deep-Sea Res.,* **45,** 1977–2010.

Nash, J. D., and J. N. Moum, 2005: River plumes as a source of large amplitude internal waves in the coastal ocean. *Nature,* **437,** doi:10.1038/nature03936.

——, E. Kunze, J. M. Toole, and R. W. Schmitt, 2004: Internal tide reflection and turbulent mixing on the continental slope. *J. Phys. Oceanogr.,* **34,** 1117–1134.

——, M. H. Alford, and E. Kunze, 2005: Estimating internal wave energy fluxes in the ocean. *J. Atmos. Oceanic Technol.,* **22,** 1551–1570.

Petruncio, E. T., L. K. Rosenfeld, and J. D. Paduan, 1998: Observations of the internal tide in Monterey Canyon. *J. Phys. Oceanogr.,* **28,** 1873–1903.

Pingree, R. D., and A. L. New, 1989: Downward propagation of internal tidal energy into the Bay of Biscay. *Deep-Sea Res.,* **36,** 735–758.

——, and ——, 1991: Abyssal penetration and bottom reflection of internal tide energy into the Bay of Biscay. *J. Phys. Oceanogr.,* **21,** 28–39.

Rainville, L., and R. Pinkel, 2006: Baroclinic energy flux at the Hawaiian Ridge: Observations from the R/P *FLIP*. *J. Phys. Oceanogr.,* **36,** 1104–1122.

Ray, R. D., and G. T. Mitchum, 1997: Surface manifestation of internal tides in the deep ocean: Observations from altimetry and island gauges. *Progress in Oceanography,* Vol. 40, Pergamon, 135–162.

Rudnick, D. L., and Coauthors, 2003: From tides to mixing along the Hawaiian Ridge. *Science,* **301,** 355–357.

Sanford, T. B., R. G. Drever, and J. H. Dunlap, 1978: A velocity profiler based on the principles of geomagnetic induction. *Deep-Sea Res.,* **25,** 183–210.

——, ——, and ——, 1985: An acoustic Doppler and electromagnetic velocity profiler. *J. Atmos. Oceanic Technol.,* **2,** 110–124.

——, E. A. D'Asaro, E. L. Kunze, J. H. Dunlap, R. G. Drever, M. A. Kennelly, M. D. Prater, and M. S. Horgan, 1993: An XCP user's guide and reference manual. Applied Physics Laboratory Tech. Rep. APL-UW TR9309, University of Washington, Seattle, WA, 59 pp. [Available from APL, University of Washington, 1013 NE 40th St., Seattle, WA 98105-6698.]

Simmons, H., R. Hallberg, and B. Arbic, 2004: Internal wave generation in a global baroclinic tide model. *Deep-Sea Res.,* **51,** 3043–3068.

St. Laurent, L., and C. Garrett, 2002: The role of internal tides in mixing the deep ocean. *J. Phys. Oceanogr.,* **32,** 2882–2899.

——, and J. D. Nash, 2004: An examination of the radiative and dissipative properties of deep ocean internal tides. *Deep-Sea Res.,* **51,** 3029–3042.

——, S. Stringer, C. Garrett, and D. Perrault-Joncas, 2003: The generation of internal tides at abrupt topography. *Deep-Sea Res.,* **50,** 987–1003.

Wunsch, C., 1998: The work done by the wind on the oceanic general circulation. *J. Phys. Oceanogr.,* **28,** 2332–2340.